Comprehensive magnetic phase diagrams of the polar metal Ca_{3}(Ru_{0.95}Fe_{0.05})_{2}O_{7}

Shiming Lei, Shalinee Chikara, Danilo Puggioni, Jin Peng, Mengze Zhu, Mingqiang Gu, Weiwei Zhao, Yu Wang, Yakun Yuan, Hirofumi Akamatsu, Moses H. W. Chan, Xianglin Ke, Zhiqiang Mao, James M. Rondinelli, Marcelo Jaime, John Singleton, Franziska Weickert, Vivien S. Zapf, and Venkatraman Gopalan

Phys. Rev. B **99**, 224411 — Published 10 June 2019

DOI: 10.1103/PhysRevB.99.224411

Comprehensive magnetic phase diagrams of the polar metal $Ca_3(Ru_{0.95}Fe_{0.05})_2O_7$

Shiming Lei[1], Shalinee Chikara[2], Danilo Puggioni[3], Jin Peng[4,5], Mengze Zhu[6], Mingqiang Gu[3], Weiwei Zhao[7], Yu Wang[4], Yakun Yuan[1], Hirofumi Akamatsu[8], Moses H. W. Chan[7], Xianglin Ke[6], Zhiqiang Mao[4,7], James M. Rondinelli[3], Marcelo Jaime[2], John Singleton[2], Franziska Weickert[2], Vivien Zapf[2], Venkatraman Gopalan[1]

Affiliations:

[1]Department of Materials Science and Engineering and Materials Research Institute, The Pennsylvania State University, University Park, Pennsylvania 16802, USA.

[2]National High Magnetic Field Laboratory, Los Alamos National Laboratory, Los Alamos, New Mexico 87545, USA.

[3]Department of Materials Science and Engineering, Northwestern University, Evanston, Illinois 60208, USA.

[4]Department of Physics and Engineering Physics, Tulane University, New Orleans, Louisiana 70118, USA.

[5]Collaborative Innovation Center of Advanced Microstructures, Laboratory of Solid State Microstructures, School of Physics, Nanjing University, Nanjing 210093, China.

[6]Department of Physics and Astronomy, Michigan State University, East Lansing, Michigan 48824, USA.

[7]Department of Physics, The Pennsylvania State University, University Park, Pennsylvania 16802, USA.

[8]Laboratory for Materials and Structures, Institute of Innovative Research, Tokyo Institute of Technology, Yokohama 226-8503, Japan

Abstract

Polar metals exist as a rather unique class of materials as they combine two seemingly mutually exclusive properties (polar order and metallicity) in one system. So far only a few polar metals have been unambiguously identified; the magnetic ones are exceptionally rare. Here we investigate a 5% Fe doped polar metal $Ca_3Ru_2O_7$, via electrical transport, magnetization, microstrain and optical second harmonic generation measurements. We report the full magnetic phase diagrams (in the field-temperature space) for magnetic field $H//a$ and $H//b$, which exhibit distinct field-dependent magnetizations behavior. In particular for $H//a$ we found a new ferromagnetic incommensurate spin structure, which is absent in the pure $Ca_3Ru_2O_7$. We propose a microscopic spin model to understand this behavior, highlighting the role of Fe doping in tipping the delicate balance of the underlying exchange interaction energy in this system.

The coexistence of magnetic and polar orders can give rise to coupled properties such as the magnetoelectric effect and multiferroicity, which could permit the mutual control of magnetism and polarization. In the past two decades much effort has been applied in designing new multiferroic materials, understanding their fundamental mechanism, and improving their magnetoelectric performance [1-12]. Khomskii [13] classifies these materials into two groups: type-I multiferroics, whose polar order and magnetism have different origins, and type-II multiferroics, for which the inversion symmetry breaking is driven by the magnetic order (this is also referred to as *spin-driven ferroelectricity*). The establishment of the magnetic phase diagram (in the field–temperature space) is an essential step towards an understanding of a new multiferroic material and its likely magnetoelectric performance. Magnetic phase diagrams have been established for many multiferroic materials, including the orthorhombic RMnO$_3$ (R = Gd, Tb, and Dy) [14], hexagonal RMnO$_3$ (R = Er, Yb, Tm, and Ho) [15], the mixed-crystal system Tb$_{1-x}$Gd$_x$MnO$_3$ [16], Ni$_3$V$_2$O$_8$ [17, 18], MnWO$_4$ [19-21], CoCr$_2$O$_4$ [22], LuFe$_2$O$_4$ [23], representative metal-organic multiferroic materials [(CH$_3$)$_2$NH$_2$]Mn(HCOO)$_3$ [24] and [CH$_3$NH$_3$]Co(HCOO)$_3$ [25], RMn$_2$O$_5$ (R = Ho, Er, Dy) [26-28], Ni$_3$TeO$_6$ [29], Lu$_2$MnCoO$_6$ [30], KCu$_3$As$_2$O$_7$(OD)$_3$ [31] and CuCrO$_2$ [32].

Conventional multiferroics are electrical insulators. However, magnetic and polar orders can also coexist in one metallic system, resulting in a magnetic polar metal. In the literature, polar metals sometimes are also called “ferroelectric” metals [33] if the polar order is switchable, in analogy to ferroelectric materials. Although only a few exist, polar metals have recently seen a renaissance in interest after the identifications of the designing rules [34, 35] and the interesting properties that they may host [36-42]. LiOsO$_3$ [43, 44], TaAs [37, 39, 40] and Ca$_3$Ru$_2$O$_7$ [42, 45-49] are three representative polar metals that have garnered recent interest. Of these three, TaAs

is not magnetic, and $LiOsO_3$ does not show any evidence of magnetic order [43]; by contrast, $Ca_3Ru_2O_7$ possesses a range of magnetically ordered phases [46, 47], that depend sensitively on temperature, applied magnetic field and field orientations. In this sense, $Ca_3Ru_2O_7$ and its derivative compounds provide a unique platform for the study of the possible interplay between the polar order and magnetic order.

In the current study, the 5% Fe-doped $Ca_3Ru_2O_7$ ($Ca_3(Ru_{0.95}Fe_{0.05})_2O_7$) is the polar metal of focus, as it was previously determined to possess an interesting incommensurate magnetic order, similar to that of many of the spin-driven multiferroic materials, such as $TbMnO_3$ [7]. As a first step towards decoding the possible interplay of magnetic and polar orders, we perform a comprehensive phase-transition study on this material using several complementary experimental tools including electrical resistivity, nonlinear optical-second-harmonic generation (SHG) [50, 51], microstrain via the Fiber-Bragg-Grating (FBG) method [52-54], and magnetometry. Here, we report measurements in DC and pulsed magnetic fields up to 25 T that fully establish the magnetic phase diagrams for field $H//a$ and field $H//b$. Following this, a comparison of $Ca_3(Ru_{0.95}Fe_{0.05})_2O_7$ with its parent system $Ca_3Ru_2O_7$ suggests a significant modification of the low-temperature magnetic phases. Particularly for field $H//a$, we find the appearance of a new ferromagnetic incommensurate spin structure and a new canted AFM-*b* (CAFM-*b*) phase in the magnetic phase diagram of $Ca_3(Ru_{0.95}Fe_{0.05})_2O_7$ that is not present in the pure $Ca_3Ru_2O_7$. This study emphasizes the role of relatively slight Fe doping (5%) in modifying magnetic interactions and eventually leading to the appearance of a new phase.

$Ca_3Ru_2O_7$ is a double-layered Ruddlesden-Popper material. Our 5% Fe-doped single-crystal samples were grown by the floating-zone method using a commercial infrared image furnace (Cannon Machinery SC2-MDH). For details of the single-crystal growth, see Ref. [55].

Recent neutron diffraction measurements suggest that $Ca_3(Ru_{0.95}Fe_{0.05})_2O_7$ retains the same space group ($Bb2_1m$) as the parent compound $Ca_3Ru_2O_7$, from room temperature to the lowest measured temperature [56, 57]. The crystal structure is illustrated in Fig. 1(a). We have examined the zero-field phase transitions by monitoring the temperature dependent resistivity [Fig. 1(b)] using a Quantum Design PPMS and the thermal expansion [Fig. 1(b) inset] using a FBG device. In a similar manner to $Ca_3Ru_2O_7$, two low-temperature transitions are observed: one at T_N = 86 K, corresponding to the Néel temperature, and the other at T_S = 40 K corresponding to a structural transition.

Since $Ca_3(Ru_{0.95}Fe_{0.05})_2O_7$ is in a polar space group ($Bb2_1m$, polar axis along b [58]), we also investigated its nonlinear optical response across these two transitions. Figure 1(c) shows the temperature dependence of the SHG coefficient d_{32}. Although $Ca_3(Ru_{0.95}Fe_{0.05})_2O_7$ shows an increased nonlinear response in d_{32} upon cooling, similar to that in $Ca_3Ru_2O_7$, the amplitude of increase is appreciably moderated in $Ca_3(Ru_{0.95}Fe_{0.05})_2O_7$. Moreover, no distinct feature is observed at T_S = 40 K in $Ca_3(Ru_{0.95}Fe_{0.05})_2O_7$, as compared to the step-wise increase of d_{32} at the structural transition temperature of T_S' = 48 K in the parent compound [Fig. 1(c)]. Such a dramatically different nonlinear optical response implies a modified electronic ground state below T_S after introducing Fe-doping into the $Ca_3Ru_2O_7$ system. This observation is consistent with a recent systematic heat-capacity study on $Ca_3Ru_2O_7$ and its doping-derivative compounds [59], where Peng *et al.* found a significantly enhanced Sommerfeld coefficient γ in $Ca_3(Ru_{0.95}Fe_{0.05})_2O_7$, attributing it to the formation of a new *localized* state that allows for the existence of a nonzero density of states (DOS) at the Fermi energy ε_F. Since the electronic state is spatially localized, an insulating/semiconducting temperature dependence is observed in the resistivity. This localized state is thought to originate from local potential fluctuations and spin-dependent fluctuations due

to the Fe doping. Considering the delicate balance between antiferromagnetic and ferromagnetic interactions in the $Ca_3Ru_2O_7$ system [56], the slight Fe-doping is likely to tip the balance of magnetic interactions and eventually introduce new magnetic phases, as we will show below. In Figs. 1(d) and (e), we also show the room temperature and low temperature SHG polarimetry [50, 60]. Symmetry analysis confirms that the polar point group of *mm*2 is retained regardless of the two observed transitions.

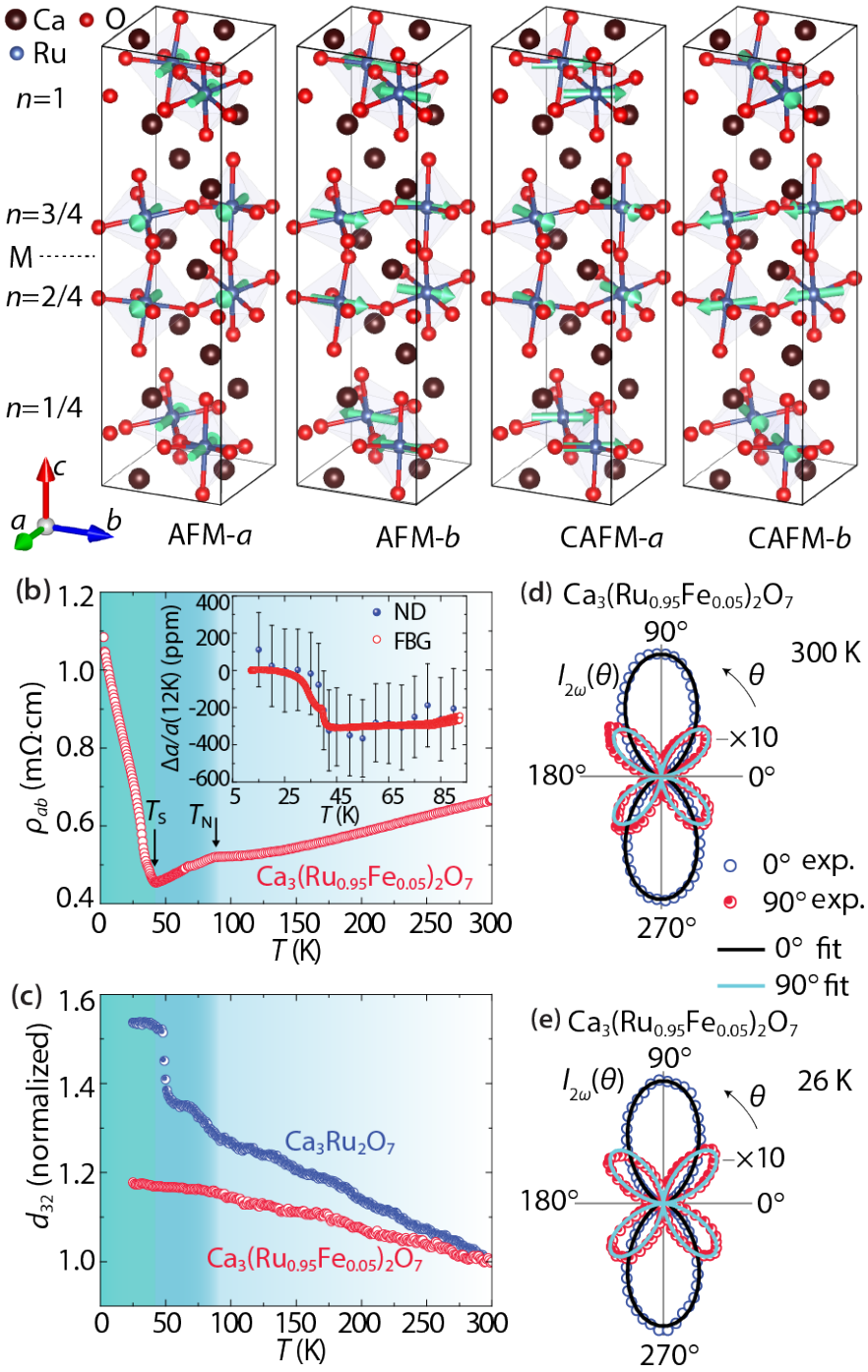

FIG. 1. Magnetic structures of $Ca_3(Ru_{0.95}Fe_{0.05})_2O_7$ and its temperature-dependent resistivity and nonlinear optical properties. (a) Illustrations of four different magnetic structures: AFM-*a*, AFM-*b*, CAFM-*a* and CAFM-*b*, in $Ca_3(Ru_{0.95}Fe_{0.05})_2O_7$. Note: in the AFM-*a* (AFM-*b*) phase, the ferromagnetic perovskite bilayers stack antiferromagnetically along *c*-axis with easy axis along *a* (*b*). In CAFM-*a* (CAFM-*b*) phase, the magnetic moment is canted so that it forms a weak ferromagnetism along *b*-axis (*a*-axis). The fractional number *n* denotes the layering coordinate of the RuO plane in one structural unit cell. The dashed line M represents a mirror symmetry. (b)

Temperature dependent in-plane resistivity (ρ_{ab}) of $Ca_3(Ru_{0.95}Fe_{0.05})_2O_7$. Two phase transitions at Ts = 40 K and T_N = 86 K are revealed. Inset shows the normalized thermal expansion and lattice parameter change, $\Delta a/a$(12 K), as a function of temperature. The blue data points are from neutron diffraction measurement, while the red data points are from FBG measurements. ppm is parts per million. (c) Temperature dependent SHG coefficient d_{32} in $Ca_3(Ru_{0.95}Fe_{0.05})_2O_7$ compared with that in pure $Ca_3Ru_2O_7$. Note: The SHG coefficient d_{32} in these two materials is normalized to the respective value at 300 K for comparison. (d) and (e) SHG polarimetry on a (001)-cleaved $Ca_3(Ru_{0.95}Fe_{0.05})_2O_7$ at 300 K and 26 K, respectively. θ is the polarization angle of the incident laser beam. The theoretical fits were performed in a *mm*2 point group symmetry at both temperatures

The DC magnetization measurements were performed on $Ca_3(Ru_{0.95}Fe_{0.05})_2O_7$ in a 7 T commercial SQUID magnetometer (Quantum Design) to understand its magnetic structure and phase transitions. Figure 2 shows the results for *H*//*a* and *H*//*b*. The field-cooling (FC) and zero-field-cooling (ZFC) curves indicate a ferromagnetic (FM) feature below T_S along the *a*-axis [Fig. 2(a)]. The existence of a FM component of the magnetization is also supported by the isothermal field-dependent magnetization measurements [Fig. 2(b)]. Comparing the *M*(*H*)-loops measured for *H*//*a* and *H*//*b*, the nonzero remanent magnetizations are observed only for *H*//*a*. These observations suggest that $Ca_3(Ru_{0.95}Fe_{0.05})_2O_7$ has a different magnetic order compared to the antiferromagnetic (AFM) ground state of the pure $Ca_3Ru_2O_7$ (Figs. S1-S3 in Supplementary Material [61], also see the reported magnetic phase diagram of $Ca_3Ru_2O_7$ in Refs. [46, 47]). Independently, neutron diffraction measurements on $Ca_3(Ru_{0.95}Fe_{0.05})_2O_7$ have revealed the emergence of incommensurate (IC) magnetic order below T_S under ZFC [56, 57]. Our magnetization measurements thus provide a complementary picture of the new magnetic order.

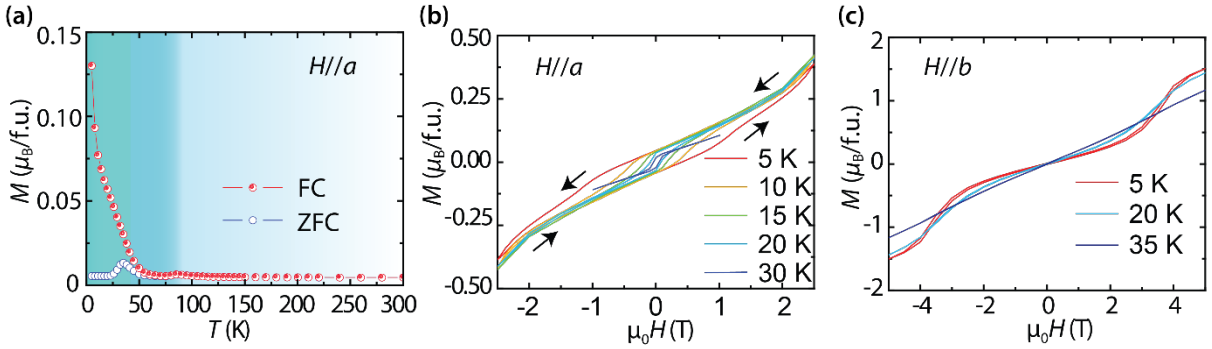

FIG. 2. DC magnetization measurements on $Ca_3(Ru_{0.95}Fe_{0.05})_2O_7$. (a) DC magnetization along *a*-axis under field-cooling (FC) and zero-field-cooling (ZFC) conditions with an applied field of 0.005 T. For the FC, condition a DC magnetic field of 5 T is applied while cooling from room temperature. (b) and (c) Isothermal field-dependent magnetization curves *M*(*H*) for *H*//*a* and *H*//*b*, respectively.

In order to establish the full magnetic phase diagrams, we have performed a high-field magnetization study using an extraction magnetometer [24] at the NHMFL's pulsed field facility at Los Alamos National Laboratory, for fields along the in-plane *a*- and *b*-axes at various temperatures ranging from 0.36 K to 90 K. The magnetization data are shown as color contour maps in Figs. 3(a), (b) for $H//a$ and Figs. 3(c), (d) for $H//b$. For better visualization of the magnetic phase-transition boundaries, we also calculated the differential magnetic susceptibility, $\chi = \mathrm{d}M/\mathrm{d}H$. Figures 3(e-h) depict the contour maps of logarithmic differential susceptibility in the H-T space. The magnetic phase diagrams shown in Figs. 4(a) and (b) are established using the magnetization and differential susceptibility maps (See Fig. S4 in Supplementary Material [61] for magnetization and differential susceptibility maps overlaid with the extracted phase-transition boundaries for the derivation of the proposed magnetic phase diagrams). Note that a coexistence of IC and AFM-*b* (IC+AFM-*b*) phases below T_S was suggested from neutron-diffraction measurements (under ZFC condition) on $Ca_3(Ru_{0.95}Fe_{0.05})_2O_7$ [56, 57]. Here we follow the same notation for the low-field state below T_S. Additionally, the magnetic transition features for both the increasing field ($H\uparrow$) and decreasing field ($H\downarrow$) are shown in Fig. 3. Comparing the phase boundaries in the differential magnetic susceptibility maps for up-sweeps and down-sweeps of the field, a slight hysteresis is observed. Other than that, these increasing and decreasing field data reflect the same phase transition physics. For brevity in discussion, the magnetic phase diagrams illustrated in Figs. 4(a) and (b) are considered only for decreasing field ($H\downarrow$) measurements. This does not affect any of the following conclusions.

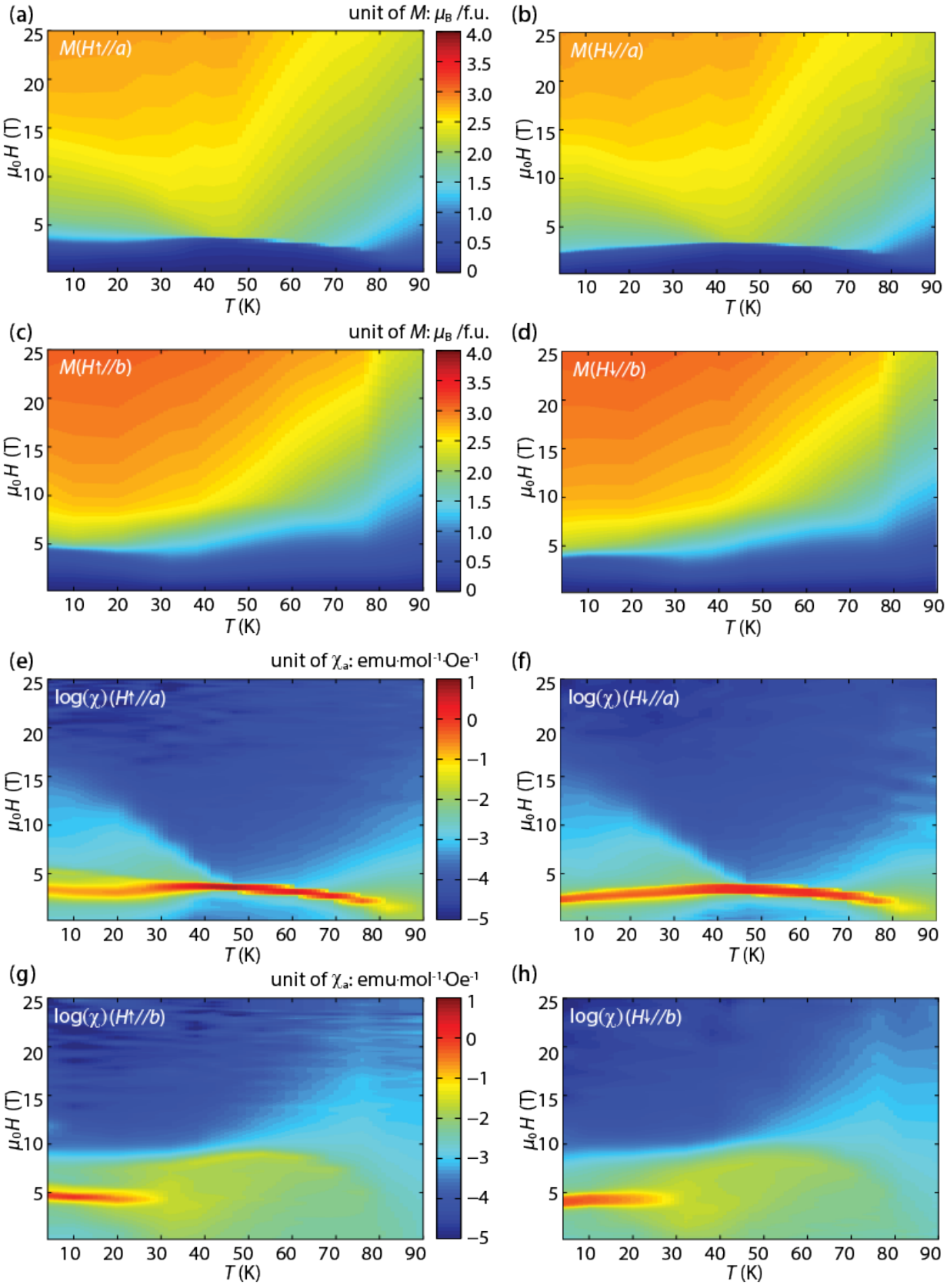
(a)
unit of M: μB /f.u.
M(H↑//a)
(b)
M(H↓//a)
(c)
unit of M: μB /f.u.
M(H↑//b)
(d)
M(H↓//b)
(e)
unit of χa: emu·mol-1·Oe-1
log(χ)(H↑//a)
(f)
log(χ)(H↓//a)
(g)
unit of χa: emu·mol-1·Oe-1
log(χ)(H↑//b)
(h)
log(χ)(H↓//b)
μ0H (T)
T (K)

FIG. 3. Contour maps of magnetization (a-d) and logarithmic differential susceptibility (e-f) of $Ca_3(Ru_{0.95}Fe_{0.05})_2O_7$. Note that the magnetization maps in (a) and (c) are measured from the increasing field sweeps, while those in (b) and (d) are from the decreasing field sweeps. The contour maps of the logarithmic differential susceptibility in (e-h) are derived from the magnetization maps in (a-d). The results shown in (a,b,e,f) are measured with $H//a$, while the results in (c,d,g,h) are measured with $H//b$. The crystallographic polar axis is along b. The field-induced spin-flop-like phase transitions are observed for both $H//a$ and $H//b$, as reflected by large differential susceptibility (redish color in (e-g)). Nevertheless, the differential susceptibility maps show clearly different magnetic transition behaviors for $H//a$ and $H//b$. Based on the information provided by the maps of magnetization and differential susceptibility, the magnetic phase boundaries are extracted for the further illustration of the magnetic phase diagrams, as shown in Fig. 4.

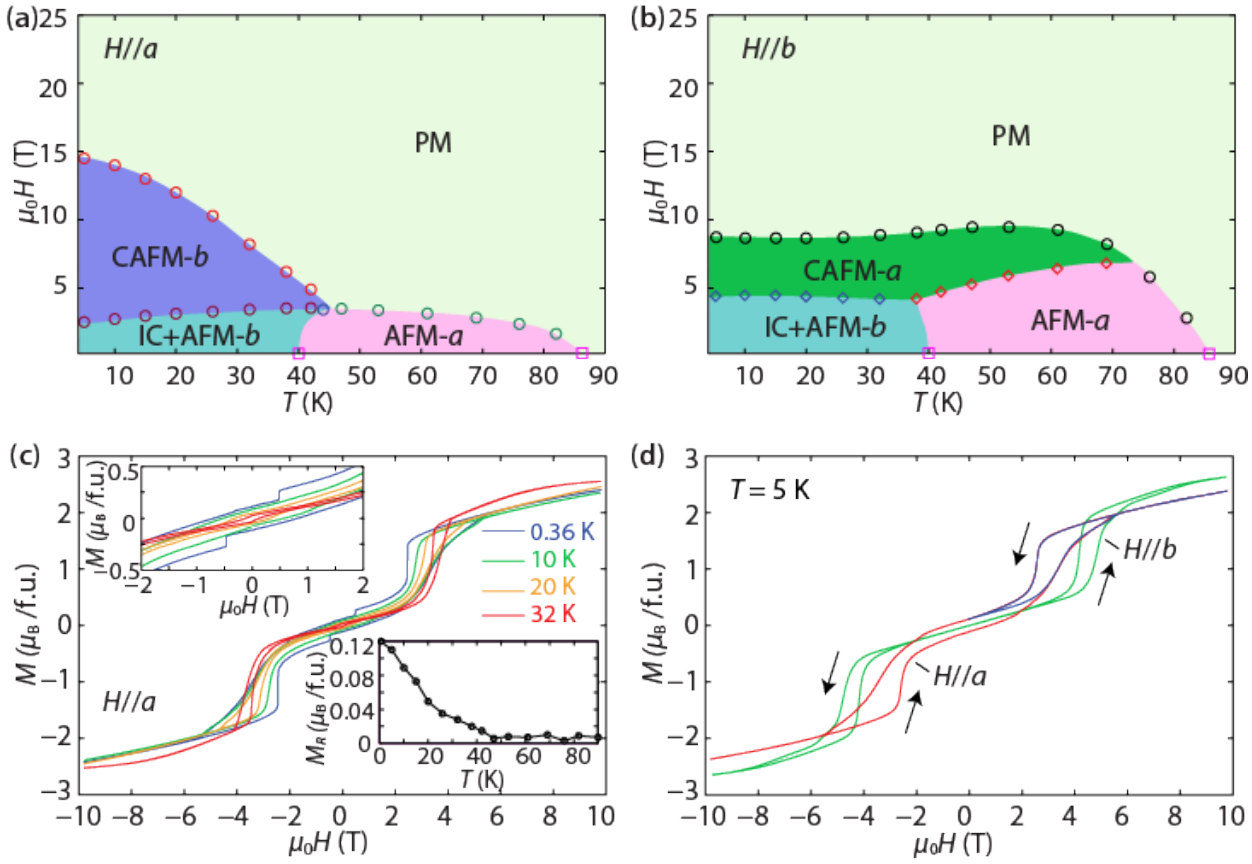

FIG. 4. Magnetic phase diagrams and $M(H)$-loops in $Ca_3(Ru_{0.95}Fe_{0.05})_2O_7$. (a) and (b) Illustrations of the magnetic phase diagrams inferred from the differential susceptibility and magnetization maps. The coordinates of circle and diamond symbols are extracted from the differential susceptibility and magnetization maps, respectively. The phase transition boundaries at low field of 100 Oe (square symbols) are determined from the temperature dependent DC magnetization and resistivity measurements. Note that the magnetic phase-transition boundaries between AFM-a and IC+AFM-b are not as precise as other boundaries, because the measurements of $M(H)$ at a constant temperature is not sensitive to the nearly vertical boundaries in the magnetic phase diagram in (a) and (b). Particularly, the phases may or may not meet at a quadruple point, and resolving it was beyond our current experimental methods. (c) $M(H)$-loops at various temperatures from pulsed magnetic field measurement along *a*-axis. Inset top-left shows a zoom-in view of opened $M(H)$-loops. Inset bottom-right shows the temperature dependent remanent magnetization after a pulse field application of +10 T. (d) A comparison of $M(H)$-loops for $H//a$ and $H//b$ at 5 K. The blue half-cycle $M(H)$-loop was obtained immediately after the red full-cycle $M(H)$-loop. Note: the high-field induced "ferromagnetic" state is denoted as paramagnetic (PM), as that in Refs. [46],[62]. IC+AFM-*b* stands for the phase coexistence of IC and AFM-*b*, as discussed in the main text.

Our results from pulsed-magnetic-field measurements are consistent with those from the DC magnetometer measurements: nonzero remanent magnetization is observed in the IC+AFM-*b* state for *H*//*a* [Fig. 4(c)] but not for *H*//*b* [Fig. 4(d)]. Additionally, the temperature-dependent remanent magnetization along the *a*-axis after applying a pulsed magnetic field of +10 T shows an upturn below ~40 K [inset bottom-right in Fig. 4(c)], which is also consistent with the field-cooled DC magnetization results shown in Fig. 2(a). From our magnetization measurements, field-induced spin-flop-like phase transitions are clear for both *H*//*a* and *H*//*b*. Zhu *et al*. [57, 63] reported the first-order incommensurate-to-commensurate (IC-to-C) magnetic transitions for field along both *a*- and *b*- axes using neutron-diffraction measurements. These transitions should correspond to the illustrated transitions of IC+AFM-*b* to CAFM-*b* or CAFM-*a* in Figs. 4(a) and (b), depending on the applied field-orientation. The neutron-diffraction measurements, however, implied that the system either remains the CAFM-*b* phase from the higher-field state after *H*//*a* is removed, or transforms into a different IC state with smaller incommensurability after *H*//*b* is removed [57, 63]. Our current complete magnetic phase diagrams suggest that such implication is not fully correct. When *H*//*a*, clear magnetic phase transitions at ≈ 2.5 T can be observed for both increasing and decreasing field sweeps. Therefore, the observed remanent magnetization for *H*//*a* should not be attributed to the persistent high-field CAFM-*b* phase. In order to reconcile our results with the neutron diffraction measurements, we propose a microscopic spin model to understand the observed ferromagnetic component when the field is removed along the *a*-axis. Since the measured FM component appears in the IC+AFM-*b* state, in sharp contrast to the pure AFM-*b* ground state in $Ca_3Ru_2O_7$, we infer that the observed nonzero magnetic moment in $Ca_3(Ru_{0.95}Fe_{0.05})_2O_7$ should be related to the unique IC phase, rather than AFM-*b* phase.

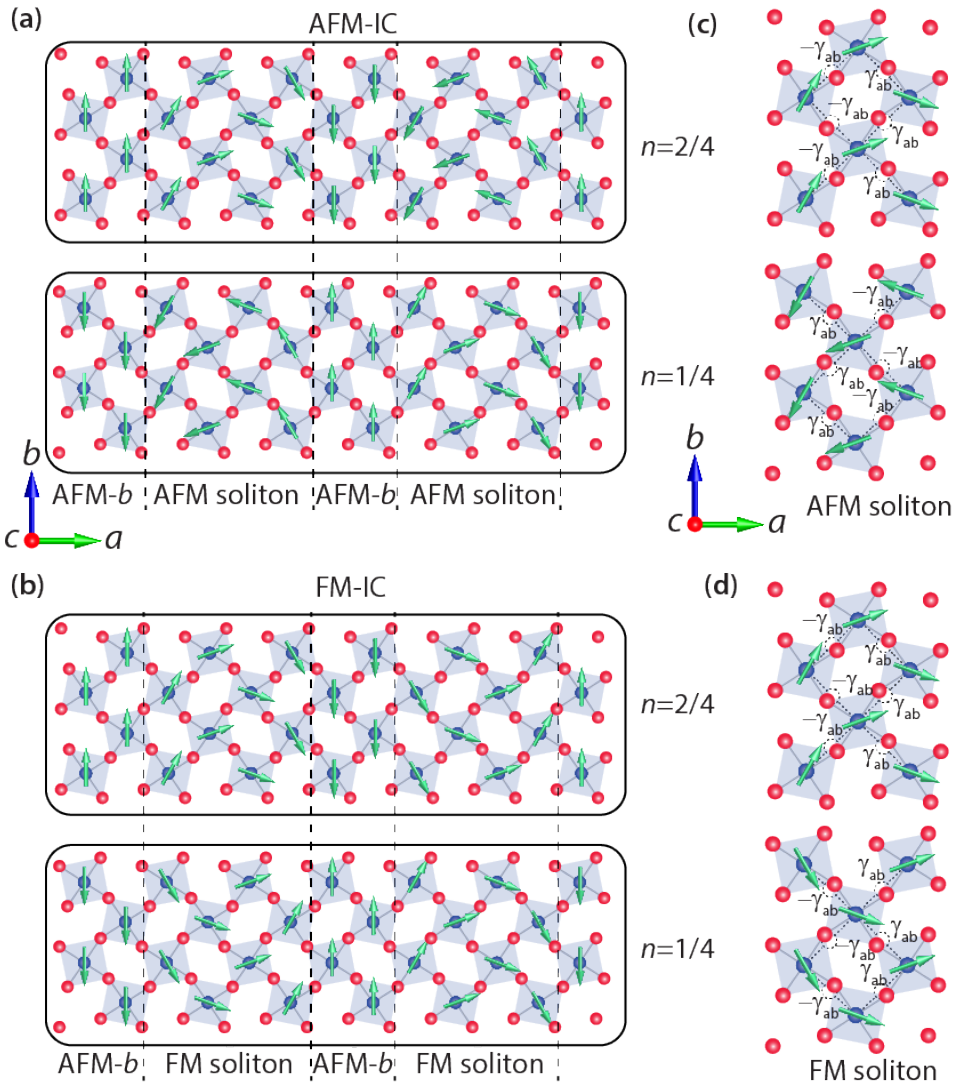

FIG. 5. Illustrations of two nearly degenerate IC magnetic structures. (a) and (b) In-plane views of the AFM-IC and FM-IC structures, respectively. Only the perovskite layers numbered 1/4 and 2/4 are shown. To a first order approximation, one period of the AFM-IC structure is composed of two anti-parallel AFM domains (AFM-*b*) and two magnetic solitons (AFM solitons) with the same chirality, while one period of the FM-IC structure is composed of two anti-parallel AFM domains (AFM-*b*) and two magnetic solitons (FM solitons) with opposite chirality. The AFM-IC has zero net magnetic moment, while FM-IC allows for the existence of a nonzero magnetic moment along *a*-axis. Note that the period of the illustrated IC structures is not to scale. The neutron-diffraction determined AFM-IC structure, for example, has a large periodicity of ~58 unit cells or ~315 Å along *a*-axis [56, 57]. (c) and (d) DM interaction analysis for the AFM soliton and FM soliton, respectively. γ_{ab} and $-\gamma_{ab}$ represent the positive and negative DM energy terms, respectively.

We next discuss the possible mechanism for observed nonzero magnetic moment in the IC phase at low temperatures. Figure 5(a) illustrates the IC spin structure determined by neutron diffraction measurements under ZFC conditions [56, 57]. The spins are parallel to each perovskite bilayer and antiparallel across each bilayer. Since there is a mirror symmetry within each bilayer (the same mirror symmetry was also shown in Fig. 1(a)), we only need to consider the spin configurations in half of the original unit cell. Figure 5 shows the in-plane view of the spin configurations in perovskite layers numbered 1/4 and 2/4. Based on the results from prior neutron-diffraction measurements, the IC structure resulting from ZFC conditions is accompanied by the formation of magnetic solitons that persist at low temperatures [56]. Therefore, the IC magnetic order within each perovskite layer is considered to form a distorted cycloidal spin structure [Fig. 5(a)]. To a first-order approximation, one period of such a distorted cycloid structure is divided into two anti-parallel AFM domains (AFM-*b*) and two magnetic solitons (AFM solitons) with the same chirality. For this spin structure, the net magnetic moment along either *a*- or *b*-axes is zero, consistent with the ZFC measurement (Fig. 2). We denote this magnetic state as AFM-IC in Fig. 5(a). Interestingly, our magnetization measurements also suggest the possible existence of a nearly-degenerate spin configuration [Fig. 5(b)]. In this magnetic structure, one of the two neighboring magnetic solitons in each perovskite layer reverses its chirality, resulting in a net nonzero magnetic moment along *a*-axis, but not along the *b*-axis, in accordance with the FC measurement (Fig. 2). We denote this state as FM-IC in Fig. 5(b).

The delicate energetic competition between the two spin configurations mentioned above can be deduced using a microscopic spin model. The Hamiltonian for a material with a single easy axis, as $Ca_3Ru_2O_7$, can be written as [10]:

$$H = \sum_{ij} J_{ij} \vec{S}_i \cdot \vec{S}_j + \sum_{i,j} \vec{D}_{ij} \cdot (\vec{S}_i \times \vec{S}_j) + \sum_i K_i (\sin \theta_i)^2. \quad (1)$$

The first term represents isotropic exchange interactions. The second term denotes antisymmetric Dzyaloshinskii-Moriya (DM) interaction [64, 65], which is principally allowed in both $Ca_3Ru_2O_7$ and $Ca_3(Ru_{0.95}Fe_{0.05})_2O_7$ due to their noncentrosymmetric structures, where the DM vector $\vec{D}_{ij} = \lambda\vec{x} \times \hat{r}_{ij}$, λ is the spin-orbit coupling constant, $\vec{x}$ is oxygen transverse shift in the Ru-O-Ru chain, and $\hat{r}_{ij}$ represents the unit vector from spins S_i to S_j. The third term represents the single ion anisotropy (SIA) where K is the anisotropy constant and θ is the angle between the local spin moment and the easy axis (b-axis below T_S).

Consider the DM interaction term. As illustrated in Fig. 5(c) and (d), the DM interactions alternate in signs along the a-axis due to the orthorhombic distortion, which is similar to the ab-plane DM interactions in the ab-cycloid phase of $Gd_{0.7}Tb_{0.3}MnO_3$ [66]. By reversing the chirality, the local DM interactions reverse their signs. However, with the alternating sign changes in the whole plane, there is no net DM energy gained or lost. Therefore, the DM interactions does not favor any of the two aforementioned magnetic structures. In the same way, the energy contribution from the SIA is the same for both spin configurations.

Next, we consider the exchange interaction term. As mentioned above, the key difference between the AFM-IC and FM-IC spin configurations is the reversed chirality in one of the two neighboring solitons within each perovskite bilayer [Fig. 5(a) and (b)]. Therefore, while the intra-bilayer nearest exchange interactions remain the same within each soliton structure, as the relative spin tilting angle remains the same [Figs. 5(c) and (d)], the inter-bilayer interactions change in response to the different inter-bilayer spin configurations [Figs. 5(c) and (d)]. In the Ruddlesden-Popper $Ca_3Ru_2O_7$ the inter-bilayer coupling is weak due to the presence of double rock-salt CaO layers [67, 68]. A similar inter-bilayer coupling is expected in 5% Fe-doped $Ca_3Ru_2O_7$ because Fe doping only has a marginal effect on the crystal structure of pristine $Ca_3Ru_2O_7$ [69]. For these

reasons, in 5% Fe-doped $Ca_3Ru_2O_7$ the two described AFM-IC and FM-IC magnetic structures [Fig. 5(a) and (b)] are expected to be nearly degenerate under zero-field condition.

When an external magnetic field is applied, the Zeeman energy ($\vec{S} \cdot \vec{B}$, where $\vec{B}$ is the local induction experienced by each individual local magnetic moment) must be added to the Hamiltonian (Eq. (1)). Thus, it becomes clear that when the applied magnetic field is along *a*-axis, the FM-IC configuration is favored over the AFM-IC one because the presence of a nonzero magnetic moment along the *a*-axis. When the magnetic field is removed, the FM-IC order survives as a metastable phase. This necessarily leads to an irreversible behavior on the field-induced magnetic order, as that observed from neutron diffraction measurements [57, 63]. The field-induced irreversibility is also seen in the resistivity for $H//a$ as shown in Fig. S5 in the Supplementary Material [61]. Based on this mechanism, no net magnetic moment can be induced for field $H//b$, although a modulation effect of the original IC structure is observed [57]. Overall, this microscopic picture suggests the existence of multiple magnetic states that are nearly degenerate in energy in $Ca_3(Ru_{0.95}Fe_{0.05})_2O_7$.

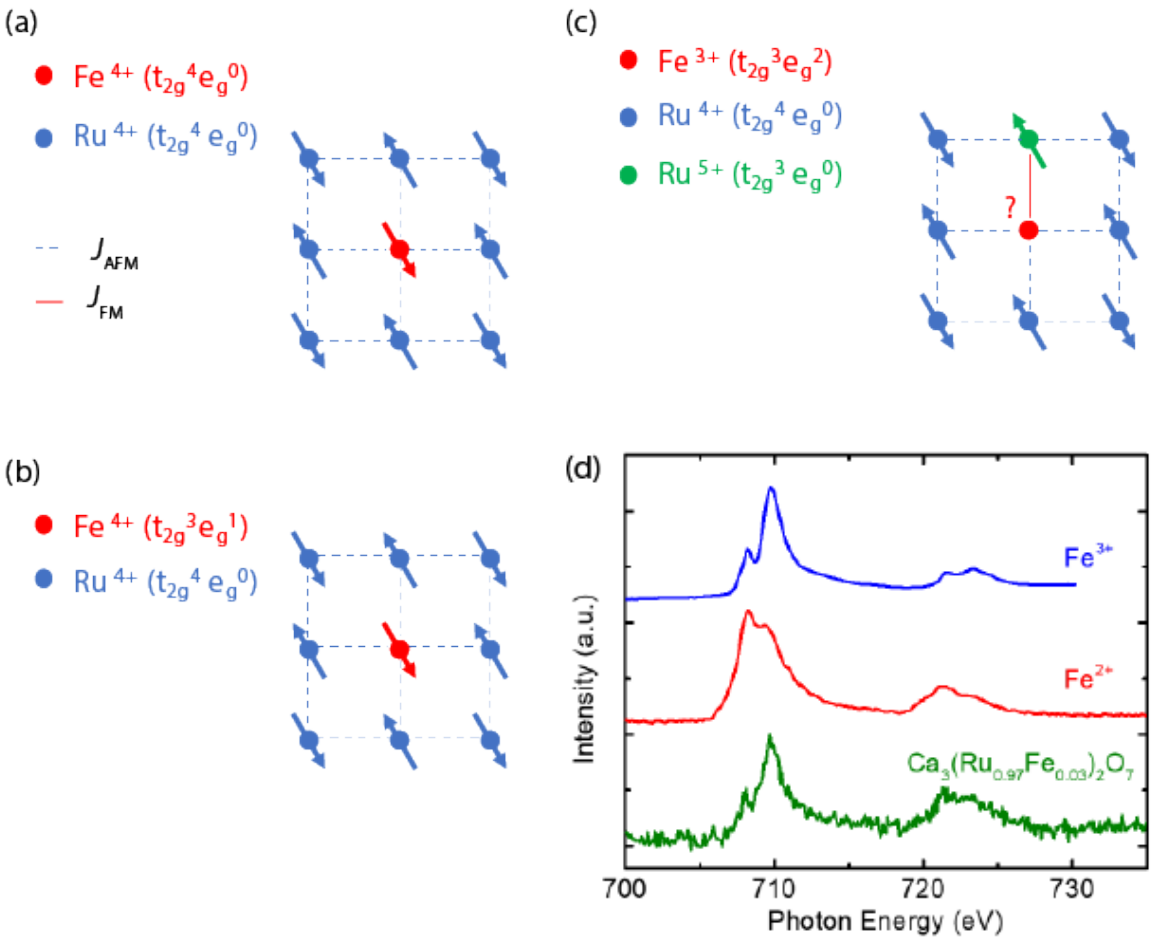

Fig. 6. Schematic illustration of the local magnetic structure around Fe^{4+} LS (a), Fe^{4+} HS (b), and Fe^{3+} (c) with Ru on nearest neighbor sites. (d) Synchrotron x-ray absorption spectroscopy of 5% Fe-doped $Ca_3Ru_2O_7$, at the Fe $L_{2,3}$ edge at room temperature, together with the results on two reference samples: FeO (Fe^{2+}) and Fe_2O_3 (Fe^{3+}).

In pure $Ca_3Ru_2O_7$, only the A-type AFM phases (AFM-*b* and AFM-*a*, see Fig. S3 in Supplementary Material [61], and the phase diagram in Refs. [46, 47]) are (thermally) accessible. The appearance of the IC magnetic phase in 5% Fe-doped $Ca_3Ru_2O_7$ reveals the important role of Fe incorporation into the lattice. To understand its role in producing the IC magnetic state, it is critical to assess the valence and spin state of Fe in $Ca_3Ru_2O_7$. Since Fe occupies a nominally Ru^{4+} lattice site, it seemly suggests that Fe should assume the same valence of Ru^{4+}; hence, serving as a substitutional cation and being a Fe^{4+} valence state. First, we note that Fe^{4+} (d^4) is quite unusual and in transition metal oxides charge disproportionation is frequently observed as $Fe^{4+} \rightarrow Fe^{3+} +$

Fe^{5+} [70-72]. Nonetheless, two spin states are in principle possible for Fe^{4+}: low spin (LS) with orbital configuration $t_{2g}^4 e_g^0$ as that in Ru^{4+} and high spin (HS) with $t_{2g}^3 e_g^1$. Second, we assume that the electronic state of Fe and its Ru next-nearest-neighbors (*nnn*) and nearest-neighbors (*nn*) are localized with well-defined local moments. With the caveats, noting that Ru^{4+} is in a LS state, and the Goodenough-Kanamori rules [73-75], we assess the magnetic symmetric exchange interactions between Ru^{4+} and Fe^{4+} cations in both the LS or HS state.

If Fe^{4+} is in a LS state, the $Fe^{4+}(t_{2g}^4)$ – O – $Ru^{4+}(t_{2g}^4)$ interaction should be AFM. Such interactions result in a magnetic structure where the *nn* spins are aligned antiparallel [Fig. 6(a)]. Note that in this specific case Fe^{4+} does not introduce any holes or oxidization effect by oxidizing Ru^{4+} into Ru^{5+}. If Fe^{4+} exhibits a HS state, then the $Fe^{4+}(t_{2g}^3)$ – O – $Ru^{4+}(t_{2g}^4)$ interaction is AFM whereas the $Fe^{4+}(e_g^1)$ – O – $Ru^{4+}(e_g^0)$ interaction should be FM. However, because Ru^{4+} is in a LS state, the AFM interaction is stronger and should dominate, giving rise to a strongly localized e_g state and the magnetic structure shown in Fig. 6(b). In addition to the two cases described above, we also consider a third case. In the Ruddlesden-Popper phase Sr_3FeRuO_7, the valence states of Fe and Ru are reported to be 3+ ($t_{2g}^3 e_g^2$) and 5+ ($t_{2g}^3 e_g^0$), respectively [76]. Therefore, a system with the combination of Fe^{3+} and Ru^{5+} appears to be favored energetically over that of Fe^{4+} and Ru^{4+}. A similar situation may be active in 5% Fe-doped $Ca_3Ru_2O_7$, and one would then need to consider the local spin environment shown in Fig. 6(c). In this local environment, the $Fe^{3+}(t_{2g}^3 e_g^2)$ cation has three *nn* $Ru^{4+}(t_{2g}^4 e_g^0)$ cations and one $Ru^{5+}(t_{2g}^3 e_g^0)$ *nn*. These orbital configurations suggest that the $Fe^{3+}(t_{2g}^3 e_g^2)$ – O – $Ru^{4+}(t_{2g}^4 e_g^0)$ interaction is AFM, whereas the $Fe^{3+}(t_{2g}^3 e_g^2)$ – O – $Ru^{5+}(t_{2g}^3 e_g^0)$ interaction is FM. In this scenario, the compound would exhibit local magnetic frustrations in the vicinity of the Fe dopant. For an experimental clue of the underlying mechanism, we resort to synchrotron x-ray absorption spectroscopy to understand the valence state of Fe. Note

that the Ru valence state is not measured due to the following two reasons: (1) the difficulty in resolving the L edge of Ru using x-ray (the L-edge energy of Ru is relatively small for hard x-ray, but relatively high for soft x-ray), and (2) the signature of the small amount of Ru^{5+} is highly likely to be overwhelmed by the dominant Ru^{4+} in the 5% Fe-doped $Ca_3Ru_2O_7$ system. Figure 6(d) show the result of x-ray absorption spectroscopy of Fe $L_{2,3}$ edge, which suggests the Fe^{3+} configuration. Therefore, we speculate that below *T*s it is the magnetic frustration due to the presence of Fe^{3+}, in combination with the magnetocrystalline anisotropy, that give rise to the detected IC magnetic ordering. In the specific case of double-layered Ruddlesden-Popper material $Ca_3(Ru_{0.95}Fe_{0.05})_2O_7$, such magnetic frustration also leads to the formation of multiple nearly degenerate magnetic states. This is essentially the origin of the observed field-induced irreversibility behavior, as well as the FM feature along *a*-axis.

In summary, by performing detailed resistivity, optical SHG, microstrain via FBG, DC magnetization, and high pulsed magnetic field measurements, we provided a comprehensive picture of the magnetic behaviors in the polar metal $Ca_3(Ru_{0.95}Fe_{0.05})_2O_7$. Particularly, we find a nonzero remanent magnetic moment for *H*//*a*, while no magnetic moment survives for *H*//*b*. We adopted a microscopic spin model to understand this behavior. It is closely related to the existence of multiple nearly-degenerate magnetic states in 5% Fe-doped $Ca_3Ru_2O_7$, suggesting a delicate balance of the intra-bilayer nearest-neighbor FM and longer-range AFM competition, and the negligible interbilayer AFM interaction. From the detailed analysis of all possible local spin configurations in the vicinity of the Fe dopant, and the experimental evidence of a Fe^{3+} state from the synchrotron x-ray absorption spectroscopy, we concluded that the magnetic frustration is the fundamental origin for the observed FM. Now that the magnetic phase diagrams are established, we look forward to identifying the possible existence of couplings between the magnetic and polar

orders in further investigations. For a polar metal system, the conventional magnetoelectric measurements might not be practical as the electric polarization is an ill-defined quantity in a metal. Therefore, we need an alternative method. One possible route is to evaluate its magnetoelastic coupling, since strain as an intermediate parameter naturally couples to both magnetic and polar orders. The behavior of the magnetoelastic response in each of the established magnetic phases will be a particularly interesting topic to pursue in the future.

Acknowledgments

Authors S.L., V.G. W. Z. and M.H.W.C. were supported by the Pennsylvania State University NSF-MRSEC Center for Nanoscale Science, under the Award Number DMR-1420620. Authors Y.Y. and V.G. were supported by DE-SC0012375. The National High Magnetic Field Laboratory is supported by the National Science foundation under cooperative Grant Nos. DMR-1157490 and DMR-1644779, the U.S. DOE, and the State of Florida. V.Z. and S.C. were supported by the Laboratory-Directed Research and Development program at LANL. J.S. is supported by the DOE BES program Science in 100 T. Authors J.P., Y.W. and Z.Q.M. were supported by the U.S. Department of Energy under EPSCoR Grant No. DE-SC0012432 with additional support from the Louisiana Board of Regents. Authors M.Z. and X.K. were supported by the National Science Foundation under Award No. DMR-1608752 and the start-up funds from Michigan State University. D.P. and J.M.R. were supported by the Army Research Office under award W911NF-15-1-0017. M.G. was supported by the U.S. Department of Energy (DOE) under Grant No. DESC0012375.

The manuscript was written through contributions of all authors. All authors have given approval to the final version of the manuscript. S.L. and V.G. conceptualized the work; J. P., Y. W. and Z.Q.M. grew the crystals; S.L., S.C., M.J., J.S., F.W. and V.Z. conducted the magnetization and

microstrain measurements under high pulsed magnetic field at LANL. S.L. and W. Z. performed the DC magnetization measurements. S.L. and Y.Y. performed the SHG measurements. M.Z. and X.K. performed the synchrotron x-ray absorption spectroscopy measurements. D.P., M.G. and J.M.R. provided the local spin configuration analysis.

REFERENCES

[1] N. A. Hill, Journal of Physical Chemistry B **104**, 6694 (2000).
[2] J. Wang, J. B. Neaton, H. Zheng, V. Nagarajan, S. B. Ogale, B. Liu, D. Viehland, V. Vaithyanathan, D. G. Schlom, U. V. Waghmare, N. A. Spaldin, K. M. Rabe, M. Wuttig, R. Ramesh, Science **299**, 1719 (2003).
[3] N. Ikeda, H. Ohsumi, K. Ohwada, K. Ishii, T. Inami, K. Kakurai, Y. Murakami, K. Yoshii, S. Mori, Y. Horibe, and H. Kitô, Nature **436**, 1136 (2005).
[4] C. J. Fennie and K. M. Rabe, Physical Review Letters **97**, 267602 (2006).
[5] H. Xiang and M.-H. Whangbo, Physical Review Letters **98**, 246403 (2007).
[6] J. H. Lee, L. Fang, E. Vlahos, X. Ke, Y. W. Jung, L. F. Kourkoutis, J.-W. Kim, P. J. Ryan, T. Heeg, M. Roeckerath, V. Goian, M. Bernhagen, R. Uecker, P. C. Hammel, K. M. Rabe, S. Kamba, J. Schubert, J. W. Freeland, D. A. Muller, C. J. Fennie, P. Schiffer, V. Gopalan, E. Johnston-Halperin, and D. G. Schlom, Nature **466**, 954 (2010).
[7] T. Kimura, T. Goto, H. Shintani, K. Ishizaka, T. Arima, and Y. Tokura, Nature **426**, 55 (2003).
[8] T. Kimura, Annu. Rev. Mater. Res. **37**, 387 (2007).
[9] I. A. Sergienko and E. Dagotto, Physical Review B **73**, 094434 (2006).
[10] M. Mochizuki and N. Furukawa, Physical Review B **80**, 134416 (2009).
[11] N. A. Benedek and C. J. Fennie, Physical Review Letters **106**, 107204 (2011).
[12] M. J. Pitcher, P. Mandal, M. S. Dyer, J. Alaria, P. Borisov, H. Niu, J. B. Claridge, and M. J. Rosseinsky, Science **347**, 420 (2015).
[13] D. Khomskii, Physics **2**, 1 (2009).
[14] T. Kimura, G. Lawes, T. Goto, Y. Tokura, and A. Ramirez, Physical Review B **71**, 224425 (2005).
[15] F. Yen, C. Dela Cruz, B. Lorenz, E. Galstyan, Y. Sun, M. Gospodinov, and C. Chu, Journal of Materials Research **22**, 2163 (2007).
[16] T. Goto, Y. Yamasaki, H. Watanabe, T. Kimura, and Y. Tokura, Physical Review B **72**, 220403 (2005).
[17] G. Lawes, A. B. Harris, T. Kimura, N. Rogado, R. J. Cava, A. Aharony, O. Entin-Wohlman, T. Yildirim, M. Kenzelmann, C. Broholm, and A. P. Ramirez, Physical Review Letters **95**, 087205 (2005).
[18] N. Wilson, O. Petrenko, and G. Balakrishnan, Journal of Physics: Condensed Matter **19**, 145257 (2007).
[19] H. Ehrenberg, H. Weitzel, C. Heid, H. Fuess, G. Wltschek, T. Kroener, J. Van Tol, and M. Bonnet, Journal of Physics: Condensed Matter **9**, 3189 (1997).

[20] K. Taniguchi, N. Abe, T. Takenobu, Y. Iwasa, and T. Arima, Physical Review Letters **97**, 097203 (2006).
[21] V. Felea, P. Lemmens, S. Yasin, S. Zherlitsyn, K. Choi, C. Lin, and C. Payen, Journal of Physics: Condensed Matter **23**, 216001 (2011).
[22] A. V. Pronin, M. Uhlarz, R. Beyer, T. Fischer, J. Wosnitza, B. P. Gorshunov, G. A. Komandin, A. S. Prokhorov, M. Dressel, A. A. Bush, and V. I. Torgashev, Physical Review B **85**, 012101 (2012).
[23] M. Phan, N. Frey, M. Angst, J. De Groot, B. C. Sales, D. Mandrus, and H. Srikanth, Solid State Communications **150**, 341 (2010).
[24] A. Clune, K. Hughey, C. Lee, N. Abhyankar, X. Ding, N. Dalal, M.-H. Whangbo, J. Singleton, and J. Musfeldt, Physical Review B **96**, 104424 (2017).
[25] L. C. Gómez-Aguirre, B. n. Pato-Doldán, J. Mira, S. Castro-García, M. A. Señarís-Rodríguez, M. Sánchez-Andújar, J. Singleton, and V. S. Zapf, Journal of the American Chemical Society **138**, 1122 (2016).
[26] D. Higashiyama, S. Miyasaka, and Y. Tokura, Physical Review B **72**, 064421 (2005).
[27] H. Kimura, Y. Kamada, Y. Noda, K. Kaneko, N. Metoki, and K. Kohn, Journal of the Physical Society of Japan **75**, 113701 (2006).
[28] C. R. Dela Cruz, B. Lorenz, Y. Sun, C. Chu, S. Park, and S.-W. Cheong, Physical Review B **74**, 180402 (2006).
[29] J. W. Kim, S. Artyukhin, E. D. Mun, M. Jaime, N. Harrison, A. Hansen, J. J. Yang, Y. S. Oh, D. Vanderbilt, V. S. Zapf, and S.-W. Cheong, Physical Review Letters **115**, 137201 (2015).
[30] S. Chikara, J. Singleton, J. Bowlan, D. A. Yarotski, N. Lee, H. Choi, Y. Choi, and V. S. Zapf, Physical Review B **93**, 180405 (2016).
[31] G. J. Nilsen, V. Simonet, C. V. Colin, R. Okuma, Y. Okamoto, M. Tokunaga, T. C. Hansen, D. D. Khalyavin, and Z. Hiroi, Physical Review B **95**, 214415 (2017).
[32] E. Mun, M. Frontzek, A. Podlesnyak, G. Ehlers, S. Barilo, S. Shiryaev, and V. S. Zapf, Physical Review B **89**, 054411 (2014).
[33] P. Anderson and E. Blount, Physical Review Letters **14**, 217 (1965).
[34] D. Puggioni and J. Rondinelli, Nature Communications **5**, 3432 (2014).
[35] T. H. Kim, D. Puggioni, Y. Yuan, L. Xie, H. Zhou, N. Campbell, P. J. Ryan, Y. Choi, J.-W. Kim, J. R. Patzner, S. Ryu, J. P. Podkaminer, J. Irwin, Y. Ma, C. J. Fennie, M. S. Rzchowski, X. Q. Pan, V. Gopalan, J. M. Rondinelli, and C. B. Eom, Nature **533**, 68 (2016).
[36] D. Varjas, A. G. Grushin, R. Ilan, and J. E. Moore, Physical Review Letters **117**, 257601 (2016).
[37] S.-M. Huang, S.-Y. Xu, I. Belopolski, C.-C. Lee, G. Chang, B. Wang, N. Alidoust, G. Bian, M. Neupane, C. Zhang, S. Jia, A. Bansil, H. Lin, and M. Z. Hasan, Nature Communications **6**, 7373 (2015).
[38] H. Weng, C. Fang, Z. Fang, B. A. Bernevig, and X. Dai, Physical Review X **5**, 011029 (2015).
[39] B. Q. Lv, H. M. Weng, B. B. Fu, X. P. Wang, H. Miao, J. Ma, P. Richard, X. C. Huang, L. X. Zhao, G. F. Chen, Z. Fang, X. Dai, T. Qian, and H. Ding, Physical Review X **5**, 031013 (2015).
[40] S. Y. Xu, C. Liu, S. K. Kushwaha, R. Sankar, J. W. Krizan, I. Belopolski, M. Neupane, G. Bian, N. Alidoust, T.-R. Chang, H.-T. Jeng, C.-Y. Huang, W.-F. Tsai, H. Lin, P. P. Shibayev, F.-C. Chou, R. J. Cava, and M. Z. Hasan, Science **349**, 613 (2015).

[41] L. Wu, S. Patankar, T. Morimoto, N. L. Nair, E. Thewalt, A. Little, J. G. Analytis, J. E. Moore, and J. Orenstein, Nature Physics **13**, 350 (2016).
[42] S. Lei, M. Gu, D. Puggioni, G. Stone, J. Peng, J. Ge, Y. Wang, B. Wang, Y. Yuan, K. Wang, Z. Mao, J. M. Rondinelli, and V. Gopalan, Nano Letters **18**, 3088 (2018).
[43] Y. Shi, Y. Guo, X. Wang, A. J. Princep, D. Khalyavin, P. Manuel, Y. Michiue, A. Sato, K. Tsuda, S. Yu, M. Arai, Y. Shirako, M. Akaogi, N. Wang, K. Yamaura, and A. T. Boothroyd, Nature Materials **12**, 1024 (2013).
[44] H. Padmanabhan, Y. Park, D. Puggioni, Y. Yuan, Y. Cao, L. Gasparov, Y. Shi, J. Chakhalian, J. M. Rondinelli, and V. Gopalan, Applied Physics Letters **113**, 122906 (2018).
[45] G. Cao, K. Abboud, S. McCall, J. Crow, and R. Guertin, Physical Review B **62**, 998 (2000).
[46] W. Bao, Z. Q. Mao, Z. Qu, and J. Lynn, Physical Review Letters **100**, 247203 (2008).
[47] S. McCall, G. Cao, and J. Crow, Physical Review B **67**, 094427 (2003).
[48] Y. Yuan, P. Kissin, D. Puggioni, K. Cremin, S. Lei, Y. Wang, Z. Mao, J. M. Rondinelli, R. D. Averitt, and V. Gopalan, Physical Review B **99,** 155111 (2019).
[49] G. Stone, D. Puggioni, S. Lei, M. Gu, K. Wang, Y. Wang, J. Ge, X.-Z. Lu, Z. Mao, J. M. Rondinelli, and V. Gopalan, Physical Review B **99,** 014105 (2019).
[50] S. A. Denev, T. T. Lummen, E. Barnes, A. Kumar, and V. Gopalan, J. Am. Ceram. Soc. **94**, 2699 (2011).
[51] T. T. A. Lummen, Y. Gu, J. Wang, S. Lei, F. Xue, A. Kumar, A. T. Barnes, E. Barnes, S. Denev, A. Belianinov, M. Holt, A. N. Morozovska, S. V. Kalinin, L.-Q. Chen, and V. Gopalan, Nature Communications **5** (2014).
[52] R. Daou, F. Weickert, M. Nicklas, F. Steglich, A. Haase, and M. Doerr, Review of Scientific Instruments **81**, 033909 (2010).
[53] M. Jaime, R. Daou, S. A. Crooker, F. Weickert, A. Uchida, A. E. Feiguin, C. D. Batista, H. A. Dabkowska, and B. D. Gaulin, Proceedings of the National Academy of Sciences **109**, 12404 (2012).
[54] G. Radtke, A. Saúl, H. A. Dabkowska, M. B. Salamon, and M. Jaime, Proceedings of the National Academy of Sciences **112**, 1971 (2015).
[55] Z. Mao, Y. Maeno, and H. Fukazawa, Materials Research Bulletin **35**, 1813 (2000).
[56] X. Ke, J. Peng, W. Tian, T. Hong, M. Zhu, and Z. Mao, Physical Review B **89**, 220407 (2014).
[57] M. Zhu, J. Peng, T. Hong, K. Prokes, T. Zou, Z. Mao, and X. Ke, Physical Review B **95**, 134429 (2017).
[58] The notation of *a*- and *b*-axes in the DC magnetization measurements in Refs. [45,47] should be switched in order to be consistent with the lattice parameter definition (lattice parameter *b*>*a*). This mislabelling mistake was previously corrected in Ref. [46]. The polar axis along *b* is also consistent with deduced polar orientation from our SHG measurement [42].
[59] J. Peng, X. Gu, G. Zhou, W. Wang, J. Liu, Y. Wang, Z. Mao, X. Wu, and S. Dong, Frontiers of Physics **13**, 137108 (2018).
[60] M. Fiebig, V. V. Pavlov, and R. V. Pisarev, Journal of the Optical Society of America B Optical Physics **22**, 96 (2005).
[61] See Supplemental Material xxx, for the magnetic phase diagrams of pure $Ca_3Ru_2O_7$, the determination of magnetic phase-transition boundaries of $Ca_3(Ru_{0.95}Fe_{0.05})_2O_7$, and the field-induced irreversibility in resistivity measurements.

[62] H. Masuda, H. Sakai, M. Tokunaga, Y. Yamasaki, A. Miyake, J. Shiogai, S. Nakamura, S. Awaji, A. Tsukazaki, H. Nakao, Y. Murakami, T. Arima, Y. Tokura and S. Ishiwata, Science Advances **2**, e1501117 (2016).
[63] M. Zhu, T. Hong, J. Peng, T. Zou, Z. Mao, and X. Ke, Journal of Physics: Condensed Matter **30**, 075802 (2018).
[64] I. Dzyaloshinsky, Journal of Physics and Chemistry of Solids **4**, 241 (1958).
[65] T. Moriya, Physical Review **120**, 91 (1960).
[66] Y. Yamasaki, H. Sagayama, N. Abe, T. Arima, K. Sasai, M. Matsuura, K. Hirota, D. Okuyama, Y. Noda, and Y. Tokura, Physical Review Letters **101**, 097204 (2008).
[67] D. J. Singh and S. Auluck, Physical Review Letters **96**, 097203 (2006).
[68] X. Ke, T. Hong, J. Peng, S. Nagler, G. Granroth, M. Lumsden, and Z. Mao, Physical Review B **84**, 014422 (2011).
[69] J. Peng, M. Q. Gu, X. M. Gu, G. T. Zhou, X. Y. Gao, J. Y. Liu, W. F. Xu, G. Q. Liu, X. Ke, L. Zhang, H. Han, Z. Qu, D. W. Fu, H. L. Cai, F. M. Zhang, Z. Q. Mao, and X. S. Wu, Physical Review B **96**, 205105 (2017).
[70] P. C. Rogge, R. U. Chandrasena, A. Cammarata, R. J. Green, P. Shafer, B. M. Lefler, A. Huon, A. Arab, E. Arenholz, H. N. Lee, T.-L. Lee, S. Nemšák, J. M. Rondinelli, A. X. Gray, and S. J. May, Physical Review Materials **2**, 015002 (2018).
[71] P. Adler, Journal of Solid State Chemistry **130**, 129 (1997).
[72] K. Kuzushita, S. Morimoto, S. Nasu, and S. Nakamura, Journal of the Physical Society of Japan **69**, 2767 (2000).
[73] J. B. Goodenough, Phys. Rev. **100**, 564 (1955).
[74] J. B. Goodenough, Journal of Physics and Chemistry of Solids **6**, 287 (1958).
[75] J. Kanamori, Journal of Physics and Chemistry of Solids **10**, 87 (1959).
[76] P. Battle, S. Bollen, and A. Powell, Journal of Solid State Chemistry **99**, 267 (1992).